Available online at www.sciencedirect.com

ScienceDirect

journal homepage: www.elsevier.com/locate/he

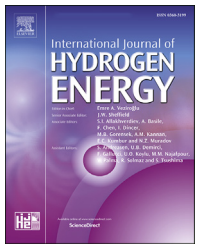

Modelling TiO_2 photoanodes for PEC water splitting: Decoupling the influence of intrinsic material properties and film thickness

A. Ansón-Casaos [a,*], J.C. Ciria [b], C. Martínez-Barón [a], B. Villacampa [c], A.M. Benito [a], W.K. Maser [a]

[a] Instituto de Carboquímica, ICB-CSIC, Miguel Luesma Castán 4, 50018 Zaragoza, Spain

[b] Department of Computer Science and Systems Engineering (DIIS), University of Zaragoza, María de Luna 1, 50018 Zaragoza, Spain

[c] Departamento de Física de La Materia Condensada. Instituto de Nanociencia y Materiales de Aragón (INMA) CSIC-Universidad de Zaragoza, Pedro Cerbuna 12, 50009 Zaragoza, Spain

HIGHLIGHTS

- Relevance of fabrication variables is proved on TiO_2 photoelectrodes.
- Film thickness and sintering atmosphere roles are investigated by data fitting.
- A theoretical model interprets trends in the cyclic voltammetry outcome.
- A phenomenological approach describes the effect on transient photocurrent.
- The change in model parameters for the photoelectrode series is discussed.

ARTICLE INFO

Article history:
Received 29 November 2022
Received in revised form
31 May 2023
Accepted 25 June 2023
Available online xxx

Keywords:
Green hydrogen
Water oxidation
Photo-electrochemical water splitting
Photoanode
Titanium dioxide

ABSTRACT

Semiconductor metal oxides are intensively studied in electrodes for photoelectrochemical (PEC) water splitting. On a series of nanoparticulate TiO_2 photoanodes, we analyze specific fabrication variables by means of data fitting. First, the experimental outcome is gathered using PEC characterization techniques, mostly cyclic voltammetry and transient photocurrent measurements. Subsequently, we apply models to gain insights into the involved charge trapping and transfer phenomena. We find that capacitance coefficients and the switch-on transient kinetics depend on the TiO_2 layer thickness, respectively indicating surface mechanisms and stationary regimes that are mediated by light accessibility. On the contrary, exponential factors of capacitance are independent of thickness, but reflect changes in the density of electron states with different sintering atmospheres. Also, the transfer resistance in the electrolyte side is indirectly influenced by sintering. Through meticulous quantitative analysis of trends, we stablish simple mathematical relationships that connect thickness-dependent parameters. This knowledge delves into fundamental mechanisms governing the TiO_2 photoelectrode behaviour, and aims to facilitate further improvements in the efficiency of materials and electrodes for green hydrogen production.

* *Corresponding author.*
E-mail address: alanson@icb.csic.es (A. Ansón-Casaos).
https://doi.org/10.1016/j.ijhydene.2023.06.284

Introduction

Water photoelectrolysis is considered as an alternative for green hydrogen production [1]. A photoelectrochemical (PEC) system consists of at least one photoactive electrode immersed in the electrolyte [2,3]. Compared to a coupled photovoltaic (PV) cell – electrolyzer (E) configuration, an integrated PEC unit allows simpler architectures, lower working voltages, and thus the possibility of using some low-cost earth-abundant components that might not work under the harsh conditions of classical electrolyzers [4]. The solar-to-hydrogen efficiency and costs of PEC and PV-E systems indicate that further improvements in the performance of photoelectrodes based on abundant materials would be decisive [5–7]. Therefore, a deep comprehension of the photoelectrochemical processes taking place in the photoelectrode is relevant for the progress in this field [8].

Most common electrochemical techniques for the characterization of semiconductor photoelectrodes include, among others, cyclic voltammetry (CV) and transient photocurrent measurements [9]. A physical model for CV plots of TiO_2 nanoparticle electrodes under dark conditions was first described by Fabregat-Santiago et al. [10] and later summarized by Berger et al. [11], assuming a connection between CV plots and the electron density of states (DOS). The model considers the classical electron DOS of a semiconductor, including conduction band, valence band, and bandgap, together with two additional types of capacitive electron trap states located inside the bandgap, which are usually associated to surface defects on TiO_2 nanocrystals [12]. The first group of trap states is just below the conduction band, and its density decreases exponentially inside the bandgap, while the second group includes isolated mono-energetic states.

Regarding transient photocurrent measurements, Peter first suggested a physical model that formally consists of a single exponential decay [13,14]. This model has been extended to a double exponential decay to properly fit certain complex phenomena, for instance those taking place in dye-sensitized photoanodes [15].

The thickness of the semiconductor layer is a critical parameter that significantly impacts the performance of the photoelectrode [16,17]. It is commonly recognized that the effect of thickness involves a delicate equilibrium between light absorption for charge generation and collection efficiency, while minimizing charge recombination [18]. Notably, previous investigations have identified optimal thicknesses that maximize photocurrent density (Table 1). It is evident that the optimal thickness is also influenced by other factors, such as chemical composition, crystal structure, deposition method, roughness, etc. [19–38]. In our experimental study, where all the electrodes are fabricated using the same protocol methodology, the influence of those parameters is considered negligible.

In the present work, we successfully apply the above-mentioned physical model for the description of CV measurements in a series of TiO_2 photoanodes, considering in detail the influence of TiO_2 layer thickness and certain processing conditions. Additionally, we develop a parametric mathematical description of transient photocurrent on the same photoanodes, introducing various characteristic times that account for different kinetic phenomena. As a whole, we reveal that effects of thickness and intrinsic material properties can be successfully decoupled into separate model parameters.

Experimental methods

The TiO_2 nanoparticles (TNPs) were synthesized by a sol-gel method from titanium isopropoxide (5 mL), using boric acid (5 mg) as an additive [39,40]. The crystallization of TNPs was performed by treatment in a horizontal reactor under air at 550 °C for 30 min. The as-prepared TNPs mostly contain anatase phase with an average crystallite size of 25 nm [40].

The crystallized TNPs were dispersed in liquid media and deposited on transparent FTO/glass substrates (70–80 Ω/sq., 80 nm). More specifically, TNPs were dispersed in an ammonia aqueous solution by an ultrasounds treatment and they were subsequently deposited using an automatic spray coating machine provided with an ultrasonic nozzle. The photoelectroactive area was of 1 cm^2. Electrodes with different thicknesses were fabricated by varying the number of cycles that the spray coating machine is depositing over the FTO/glass substrate. Electrodes were finally sintered at 450 °C for 2 h in either nitrogen or air atmospheres.

In the following, sample nomenclature includes abbreviations standing for the dispersion liquid (W for water) and the sintering atmosphere (N for nitrogen, A for air). In this way, electrodes are called TNP-W-N or TNP-W-A, followed by the TiO_2 layer thickness in μm. For comparison, we also prepared an electrode by dispersion of the TNPs in isopropanol (abbreviated as I) and subsequent spray coating with a manual gun [41]. Fitting parameters that will be presented for the TNP-I-A-2.0 μm optimized electrode are well-consistent mathematically and can be thus compared with those of series TNP-W-N and TNP-W-A.

Scanning electron microscopy (SEM) images were obtained by means of secondary electrons using the JEOL JSM 6400 Scanning Electron Microscope. Thickness of the samples, as well as the roughness of their surface, were evaluated by using a contact DektakXT Stylus Profiler (from Bruker). The radius of the stylus used in the measurements was 2.5 μm. The height of the step of the TiO_2 layer was measured in different areas along the layer edge. The depths of grooves made in different parts of the layer (reaching the substrate) were also determined. The electrode thickness was obtained as the mean value of such measurements.

Electrochemical measurements were performed in a 3 electrode glass cell provided with a quartz window, using a PGSTAT302 N potentiostat (Metrohm Autolab). The reference electrode (RE) was Ag/AgCl (3 M NaCl, $E^\circ = 0.210$ vs. SHE) and the counter electrode (CE) was a graphite rod. The electrolyte was 0.1 M Na_2SO_4. A 150 W Xe arc lamp (Quantum Design GmbH), providing AM1.5G illumination, was utilized for the

Please cite this article as: Ansón-Casaos A et al., Modelling TiO_2 photoanodes for PEC water splitting: Decoupling the influence of intrinsic material properties and film thickness, International Journal of Hydrogen Energy, https://doi.org/10.1016/j.ijhydene.2023.06.284

Table 1 – Literature studies that directly indicate an optimization of the photoactive film thickness on the photoelectrode, paying particular attention to TiO_2 as the semiconductor.

Material	Deposition method	Thickness range [μm]	Optimal thickness [μm]	J_{ph} [mA·cm^{-2}]	Reference
TiO_2 (A)	Dip coating	3.3–15	15	0.25	[19]
Ta–TiO_2 (A + R)	Electrochemical	3–12	7	0.55	[20]
TiO_2 (B + R + A)	Supersonic aerosol	0.5–4	3	0.09	[21]
TiO_2 (A)	Spray pyrolysis	0.34–0.80	0.80	0.13	[22]
TiO_2/B-diamond	RF sputtering	0.3–1	0.66	3.38	[23]
TiO_2 (A)	Pulsed laser	0.50–3.60	1.4	0.13	[24]
TiO_2 (A + R)	Electrophoresis	5–35	14.7	2.12	[25]
TiO_2 (A + R)	CVD	0.1–11	0.6	1.2	[26]
TiO_2 (A)	Screen printing	2.67–9.92	4.89	0.33	[27]
TiO_2 (A + R)	Dip coating	4–11	4	0.03	[28]
TiO_2 (A)	Dip coating	0.45–2.15	2.15	0.20	[29]
TiO_2 (A)	Atomic layer deposition	0.01–0.09	0.05	0.14	[30]
Zn–Fe_2O_3/Fe –TiO_2	Spray pyrolysis	0.24–1.21	0.89	0.75	[31]
Fe,Al-WO_3	Magnetron sputtering	0.03–0.83	0.45	0.03	[32]
α-Fe_2O_3	Spray pyrolysis	0.01–0.03	0.03	0.26	[33]
$BiVO_4$	Dip coating	0.06–0.21	0.16	0.57	[34]
CuO_2/CeO_2	Spray pyrolysis	0.10–0.49	0.40	2.89	[35]
$BiVO_4$	Electrodeposition	0.06–0.52	0.48	0.45	[36]
Fe,Ni–Co_3O_4	Spray pyrolysis	0.14–2.16	2.16	−4.14	[37]
Ti–Fe_2O_3	Hydrothermal	0.18–0.65	0.52	2.0	[38]

PEC tests. All the CV experiments were performed at a scan rate of 20 mV s^{-1}, starting at 0.4 V vs. Ag/AgCl. All the transient photocurrent measurements were run at 0.4 V vs. Ag/AgCl for 5 min, with chopping light intervals of 15 s, resulting in 10 on-off pulses.

Model description

Cyclic voltammetry in the dark

We apply well-established models of CV under dark conditions [10,11], with the aim of extracting new information about the influence of certain electrode fabrication variables, including thickness. The circuit used for CV measurements is sketched in Fig. 1a. The potential of the RE remains fixed. A potentiostat adjusts the overall potential (V_s) so as to ensure that the potential difference (V) between the working electrode (WE) and the RE is linearly swept with time back and forth between two pre-set limits V_1 and V_2. In our measurements, $V_1 = 0.4$ V and $V_2 = -1.1$ V, and the scan rate is $s = 20$ mV/s.

Fig. 1b sketches the relevant energy levels, following general definitions that were introduced by Bisquert et al. [42]. The potential V is related to the difference between the electron Fermi level at the back contact of the WE and the energy of the RE ($\varepsilon_{Fn;b} - \varepsilon_{RE} = -q_e V$). It is convenient to relate both the Fermi level and V to their values under equilibrium, where the electron Fermi level equals the redox level in the electrolyte ($\varepsilon_{Fn;0} = \varepsilon_{redox}$, $\varepsilon_{Fn;0} - \varepsilon_{RE} = -q_e V_0$). The displacement of the electron Fermi level in the WE can be related to a voltage V_{app}:

$$V_{app} \equiv V - V_0 = \frac{\varepsilon_{Fn;0} - \varepsilon_{Fn;b}}{q_e} \quad \text{Eq. 1}$$

In order to describe the intrinsic capacity of the WE and the charge transfer between the WE and the electrolyte, we refer to the model described in Refs. [10,11], which we briefly summarize in the following. Besides the conduction and valence band edges of the semiconductor, with energies ε_c and ε_v respectively, the TiO_2 capacitance is related to the occupancy of electron trap states inside the bandgap. The occupancy depends on the density of states (g) and the probability that they are occupied, given by the Fermi-Dirac distribution (f). More precisely, the electron density n is given by:

$$n = \int g(\varepsilon) f(\varepsilon - \varepsilon_{Fn})\, d\varepsilon \quad \text{Eq. 2}$$

Capacitance expresses the dependence of the trapped charge on the potential:

$$C = \frac{d\,Q}{d\,V} = {q_e}^2 \frac{dn}{d\varepsilon_{Fn;b}} \quad \text{Eq. 3}$$

Two types of electron trap states are considered: continuous and monoenergetic trap states, with energies ε_{cts} and ε_{mts} respectively. The continuous traps are shallow defect states, which are responsible for an exponential decrease in the DOS of the conduction band towards the bandgap. They may be associated to vacancies in the TiO_2 lattice. Their density of states is given by:

$$g_{cts}(\varepsilon) = \frac{\Theta_{cts}}{K\,T_c} \exp\left(\frac{\varepsilon - \varepsilon_{c;s}}{K\,T_c}\right) \quad \text{Eq. 4}$$

where Θ_{cts} stands for the volume density of band tail states, T_c is a parameter modelling their broadening, and $\varepsilon_{c;s}$ is the energy of the conduction band edge at the surface of TiO_2. Their associated capacitance is obtained by substituting Eq. (4) into Eq. (2) and applying Eq. (3). It can be approximated by its value at low temperature, where the Fermi-Dirac distribution tends

Please cite this article as: Ansón-Casaos A et al., Modelling TiO_2 photoanodes for PEC water splitting: Decoupling the influence of intrinsic material properties and film thickness, International Journal of Hydrogen Energy, https://doi.org/10.1016/j.ijhydene.2023.06.284

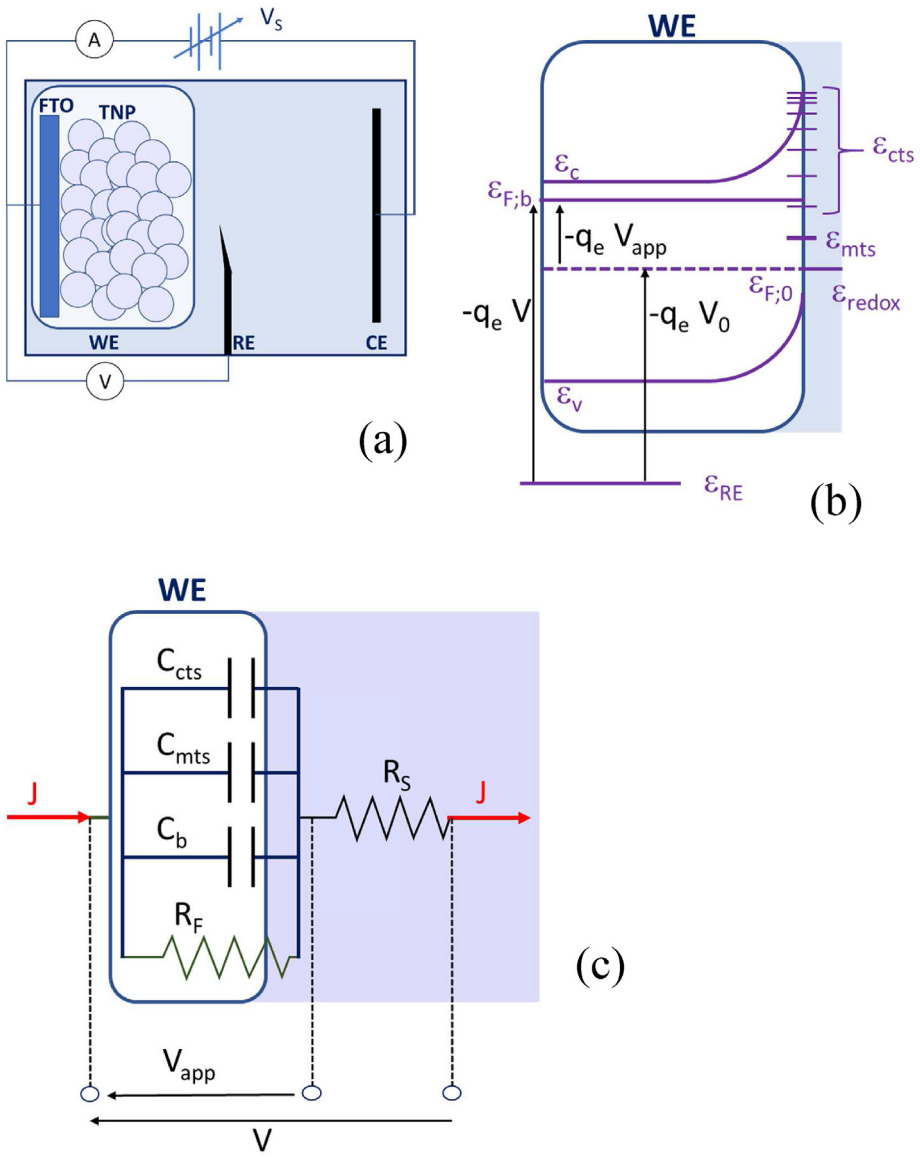

Fig. 1 – Schema of the model elements of CV measurements in the dark: a) The 3-electrode cell with working, reference and counter electrodes (WE, RE, CE); b) Energy levels of the WE; and c) Model circuit for the WE.

to the Heaviside step-function $H(\varepsilon_{Fn} - \varepsilon)$. Since we are interested in the capacitance per unit area, we multiply the resulting expression by h, the thickness of the electrode:

$$C_{cts} \sim h\, q_e{}^2\, \frac{\Theta_{cts}}{K\, T_c}\, \exp\left(\frac{\varepsilon_{Fn;b} - \varepsilon_{c;s}}{K\, T_c}\right) = C_a\, \exp\left(-\frac{\alpha_c\, V_{app}}{V_T}\right) \quad \text{Eq. 5}$$

where $C_a = h\, q_e{}^2\, \frac{\Theta_{cts}}{K\, T_c}\, \exp\left(\frac{\varepsilon_{Fn;0} - \varepsilon_{c;s}}{K\, T_c}\right)$, $\alpha_c = T/\, T_c$ and $V_T = \frac{K\, T}{q_e}$ is the thermal voltage.

On the other hand, the monoenergetic traps are deep defect states, which are responsible for producing rather isolated energetic states in the bandgap region of TiO_2, and are typically associated to doping and grain-boundary effects [43]. The volume density of a monoenergetic state of energy ε_{mts} is given by the Dirac delta distribution,

$$g_{mts}(\varepsilon) = N_{mts}\, \delta(\varepsilon - \varepsilon_{mts}) \quad \text{Eq. 6}$$

and thus its associated capacitance per unit area is:

$$C_{mts} = h\, q_e{}^2\, \frac{N_{mts}}{K\, T}\, \frac{\exp\left(\frac{\varepsilon_{mts} - \varepsilon_{Fn}}{K\, T}\right)}{\left(1 + \exp\left(\frac{\varepsilon_{mts} - \varepsilon_{Fn}}{K\, T}\right)\right)^2} = C_m \frac{\exp\left(\frac{V_{app} - E_{mts}}{V_T}\right)}{\left(1 + \exp\left(\frac{V_{app} - E_{mts}}{V_T}\right)\right)^2} \quad \text{Eq. 7}$$

where $E_{mts} = \frac{\varepsilon_{F0} - \varepsilon_{mts}}{q_e}$ and $C_m = h\, q_e{}^2\, \frac{N_{mts}}{K\, T}$.

A third capacitive term C_b is added to take into account the remaining capacitance at high V_{app} values, when both C_{cts} and C_{mts} are very low.

The faradaic charge transfer process at the nanoporous electrode-electrolyte interface is modelled by a resistance in

Please cite this article as: Ansón-Casaos A et al., Modelling TiO_2 photoanodes for PEC water splitting: Decoupling the influence of intrinsic material properties and film thickness, International Journal of Hydrogen Energy, https://doi.org/10.1016/j.ijhydene.2023.06.284

parallel R_F that tends to a constant value at sufficiently high negative voltage values [10]:

$$R_F = R_{Fa}\, exp\left(\frac{\alpha_R\, V_{app}}{V_T}\right) + R_{Fb} \quad \text{Eq. 8}$$

The exponential dependence of R_F on V_{app} can be justified by inspecting Fig. 1b. The more negative V_{app}, the closer ε_{Fn} gets to $\varepsilon_{c;s}$ and thus the greater density of free electrons, which is an increasing exponential function of $\varepsilon_{Fn} - \varepsilon_{c;s}$.

In summary, the intrinsic capacitive and charge transfer phenomena in the WE are modelled by a circuit consisting of three capacitors and a resistance in parallel, represented in Fig. 1c. In addition, a series resistance R_s is included to consider the resistivity at the substrate-wire contact, as well as the intrinsic resistance in the electrode and the electrolyte between the WE and RE.

The current density crossing the model circuit (see Fig. 1c) is:

$$J = C\frac{dV_{app}}{dt} + \frac{V_{app}}{R_F} = (C_{cts} + C_b + C_{mts})\frac{dV_{app}}{dt} + \frac{V_{app}}{R_F} \quad \text{Eq. 9}$$

The dynamics of the model circuit is ruled by the equation:

$$\frac{dV_{app}}{dt} = \frac{1}{CR_S}\left(V - V_{app}\frac{R_S + R_F}{R_F}\right) \quad \text{Eq. 10}$$

Transient photocurrent

We propose a mathematical fitting to describe the kinetics of various phenomena that are observed in transient photocurrent measurements. The response to a pulse of light consists of a current spike followed by a plateau that exhibits a progressive decay. The spike is fitted to a function of the form:

$$J_{spike}(t) \equiv J_{spike}(J_p, t_0, \tau_0;\ t) = J_p\left(1 - e^{-\frac{t-t_0}{\tau_0}}\right) \quad \text{Eq. 11}$$

where J_p is the pulse maximum, t_0 the starting time, and τ_0 is a characteristic time: the lower τ_0, the higher dJ/dt, and thus the shorter it takes for the current to reach its peak.

The subsequent relaxation plateau is fitted to a biexponential decay whose shape is given by:

$$J_{plateau}(t) \equiv J_{plateau}(J_f, A_1, \tau_1, A_2, \tau_2, t_{p0}\,;t) = J_f + A_1\, e^{-\frac{t-t_{p0}}{\tau_1}} + A_2\, e^{-\frac{t-t_{p0}}{\tau_2}} \quad \text{Eq. 12}$$

t_{p0} being the time at which the photocurrent reaches its peak. Eq. (12) implies the existence of two relaxation phenomena with characteristic times τ_1 and τ_2, while A_1 and A_2 give an estimation of the relative intensity of both phenomena.

Results and discussion

Experimental outcome

The morphological study of selected TiO_2 electrodes is presented in Fig. 2. The thermal treatment at 450 °C leads to a significant degree of nanoparticle sintering in all TiO_2 films. Detailed examination of SEM images and profile scans reveals that the films prepared by the automatic spray coating machine (TNP-W-A-3.2 μm and TNP-W-N-3.1 μm) exhibit strong roughness. This roughness is primarily attributed to the use of a spray technology employing an ultrasound nozzle to generate the spray, since the films obtained using a manually applied gun (TNP-I-A-2.0 μm) show a smoother surface. Interestingly, the choice of sintering atmosphere, whether air or nitrogen, does not result in remarkable qualitative effects on the surface morphology.

Mean values of the film thickness were obtained from contact profilometry scans. Additionally, roughness values were quantified. As stated in the experimental section, electrodes of distinct thicknesses were prepared performing a different number of spray coating cycles. For a relatively low number of cycles, less homogeneous coatings were obtained, giving rise to roughness values of higher than those for thicker samples. Film roughness ranging from 0.6 to 1.3 μm were obtained for electrodes in the TNP-W-N series, while, as a rule, the TNP-W-A series showed slightly lower roughness values (<1 μm). As an exception, the thinnest electrodes in the TNP-W-A series showed roughness values above 1.2 μm.

Typical examples of the raw PEC experimental data are presented in Fig. 3. In the dark, CV shows a charge accumulation region at $E < -0.7$ V vs. Ag/AgCl, which is equivalent to < -4.0 eV in the reference vacuum scale and approximately indicates the energy level of the TiO_2 conduction band. An increase in the intensity of the charge accumulation region with thickness is observed comparing thin and thick electrodes (Fig. 3a and 3b). As an example, a 3-fold increase is observed from the TNP-W-N-2.5 μm to the TNP-W-N-14.6 μm electrode at −1 V vs. Ag/AgCl.

Under light irradiation, a photocurrent is observed in CV scans at $E > -0.2$ V, reaching a plateau in the range of 0–0.4 V vs. Ag/AgCl (Fig. 3a and 3b). In this work, we choose to perform transient photocurrent measurements at 0.4 V vs. Ag/AgCl. The charge accumulation region is distorted and increases its intensity by 1.3–1.6 times upon irradiation.

Transient photocurrent measurements under intermittent irradiation are presented in Fig. 3 c for selected TNP-W-N electrodes of distinct thickness. The chopping interval is 15 s and the total experiment time 5 min, thus generating 10 on-off pulses for each sample. Fig. 3 d includes the complete set of photocurrent values after 5 min, at the end of the 10th pulse. In agreement with previous literature (Table 1), a maximum photocurrent is observed as a function of the TiO_2 layer thickness. The trend is clearly identified for samples sintered in N_2 atmosphere, since a large number of samples of different thicknesses was analyzed.

The shape of photocurrent pulses clearly depends on the TiO_2 layer thickness (Fig. 3c). Photocurrent spikes are observed just after switching on the light for thin TiO_2 layers, while spikes do not appear in thick electrodes. In any case, negative overshoots are not observed after switching off the light. This fact might indicate relatively high rates for the chemical reaction of photogenerated holes, according to kinetic simulations performed by Araujo et al. [44].

Fitting CV in the dark

The fitting procedure consists in finding the parameter values that minimize a given error function measuring the difference between model estimations and experimental data:

Please cite this article as: Ansón-Casaos A et al., Modelling TiO_2 photoanodes for PEC water splitting: Decoupling the influence of intrinsic material properties and film thickness, International Journal of Hydrogen Energy, https://doi.org/10.1016/j.ijhydene.2023.06.284

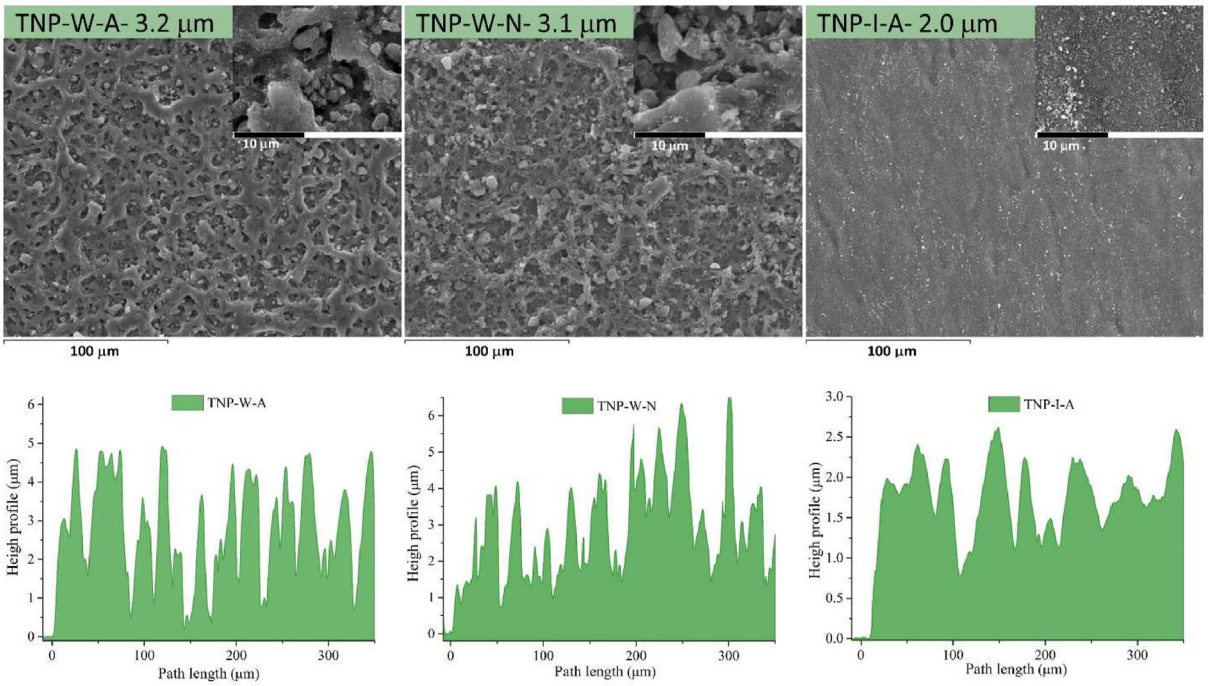

Fig. 2 – Morphological characterization of three selected TiO_2 electrodes. SEM images correspond to two different magnification values: ×500 (100 μm scale bar) and ×5000 (10 μm scale bar). The bottom part includes representative profilometer scans.

$$p^* = argmin_p \left\| J_{exp} - J_{estim}(p) \right\| \quad \text{Eq. 13}$$

In our case, $p = \{C_a, \alpha_C, C_b, C_m, E_{mts}, R_{Fa}, \alpha_R, R_{Fb}, R_s\}$ is the set of parameters defined in Section, p^* the set of values that actually minimize Eq. (13), J_{exp} the measured values of the current density, and $J_{estim}(p)$ the solution of Eqs. (9) and (10) as a function of the parameters. In particular, Eq. (9) was solved by means of the 4th order Runge-Kutta method. Starting from an initial guess of the values of p, their final values were estimated applying the Levenberg-Marquadt algorithm [45].

According to Eq. (5), α_C is independent of the sample thickness. An analogous behaviour can be expected for α_R (Eq. (8)). To check whether our results support that idea, we followed a two-step process. In the first step, the fitting was carried out independently for each sample and, indeed, both α_C and α_R showed nearly identical values for samples with different thickness, while the other parameters exhibited a clear variance between samples. In the second step, we forced common values of α_C and α_R for all the samples within a given series (TNP-W-N or TNP-W-A). For each sample, the fitting error (Eq. (13)) in this second step is less than 1% larger than the error computed in the first step, when the parameters are allowed to freely change from sample to sample. We can conclude that α_C and α_R depend on intrinsic material characteristics that can be related to the preparation process, but are independent of the sample thickness.

Comparison of the fitting curve with the original CV data reveals the successful application of the model for both thin and thick electrodes (Fig. 4a and 4b). The resulting values for the complete set of electrodes are summarized in Table 2. The fitting outcome shows interesting trends with respect to the TiO_2 layer thickness (Fig. 4c and 4d). According to Eqs. (5) and (7), C_a and C_m would be expected to be linear functions of the thickness h. However, our results suggest that they both increase linearly for small h values and saturate for thick samples. A simple function that mimics the observed behaviour is an asymptotic exponential function:

$$C_a = C_{a,0}\left(1 - e^{-\frac{h}{L_a}}\right) \quad \text{Eq. 14}$$

$$C_m = C_{m,0}\left(1 - e^{-\frac{h}{L_m}}\right) \quad \text{Eq. 15}$$

where $C_{a,0}$, L_a, $C_{m,0}$, and L_m are fitting parameters (Table 2). This trend reasonably indicates that C_a and C_m coefficients are associated with surface phenomena. For thin TiO_2 layers, the capacitance linearly increases with thickness since the surface that is accessible to the electrolyte increases. Indeed, that would correspond to limiting phenomena contemplated by Eq. (5). However, for thick electrodes, the capacitance saturates at a certain level, when no additional surfaces can be reached by the liquid, and this is what is observed and described as non-intrinsic thickness phenomena.

The change in the third capacitive term C_b does not saturate and might be linear in the whole considered range of thickness (Fig. 4c):

$$C_b = C_{b,0} \cdot h / L_0 \quad \text{Eq. 16}$$

Please cite this article as: Ansón-Casaos A et al., Modelling TiO_2 photoanodes for PEC water splitting: Decoupling the influence of intrinsic material properties and film thickness, International Journal of Hydrogen Energy, https://doi.org/10.1016/j.ijhydene.2023.06.284

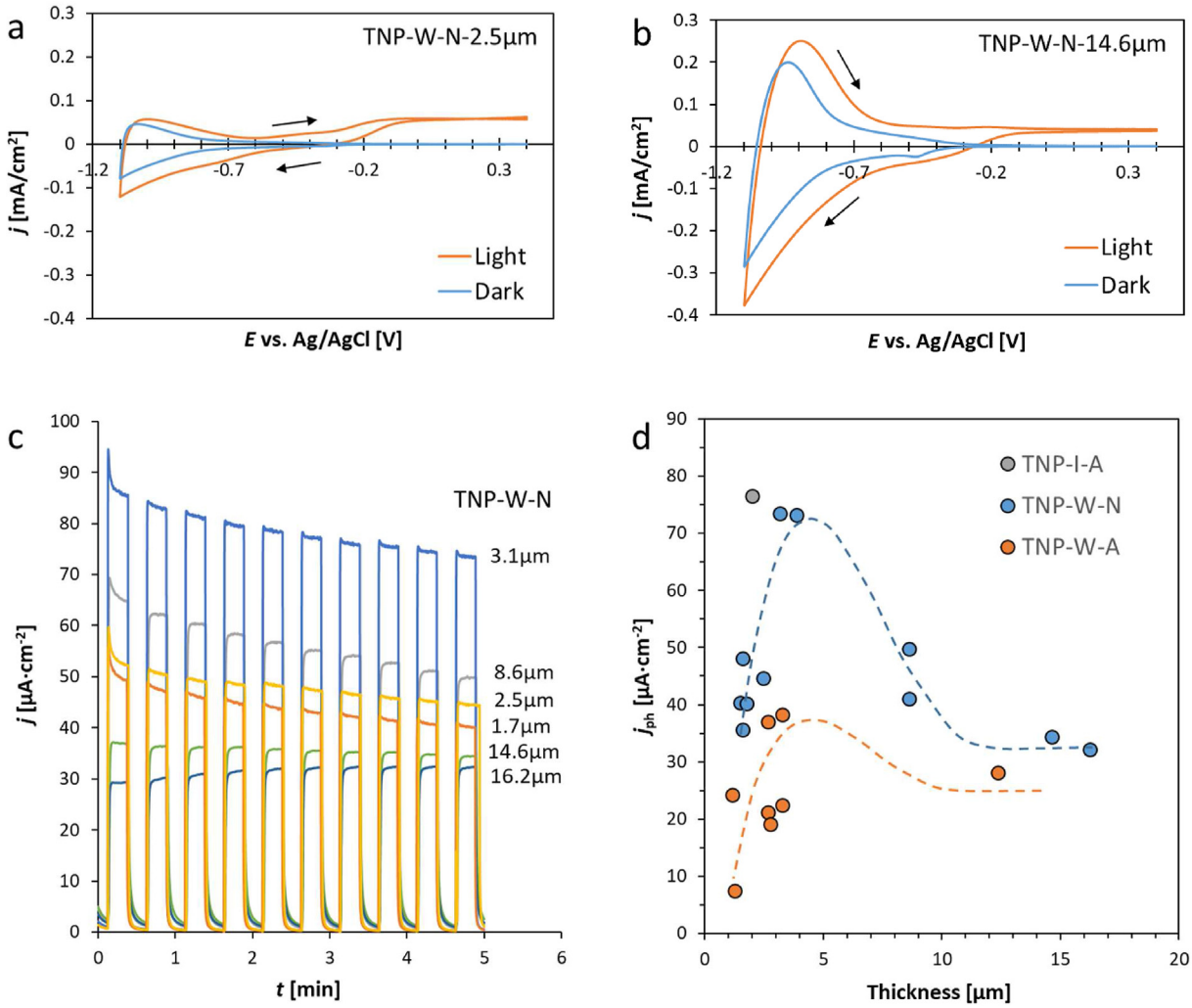

Fig. 3 – Representative PEC experimental results: a, b) CV in the dark and under light irradiation (20 mV s^{-1}, starting at 0.4 V), on film electrodes of different thickness; c) transient photocurrent measurements at 0.4 V on various samples of the TNP-W-N series of electrodes; d) photocurrent values (j_{ph}) after 5 min of chopped light irradiation, as a function of thickness, discontinuous lines being eye guides.

where $L_0 = 1$ µm is a normalization factor. Therefore, the characteristic parameter $C_{b,0}$ (Table 2) does not depend on the electrochemically active surface, but on intrinsic bulk properties such as the crystalline structure of TiO_2 particles. Besides, the clearly different trends of C_a and C_b with thickness supports the need of introducing the C_b contribution. The original model properly describes intrinsic characteristics when $h \ll L_a$ but no thickness-dependent saturation effects are foreseen. We include the extrinsic thickness influence, being able to model it successfully. We see the saturation of C_a and C_m at high thickness, as well as the need for bringing in a thickness dependent C_b term, all this for thicknesses beyond $h \ll L_a$. Therefore, it is deduced that thickness effects have to be contemplated in models of real photoanode structures.

Because of the contribution of C_{mts}, the capacitance has a local maximum when $V_{app} = E_{mts}$ (Eq. (7)), which can be observed around −0.25 V (Fig. 4a and 4b). Unlike in our simulation, the measured current only shows a well-defined peak when charging the electrode, but not in the subsequent discharge. This asymmetry can be explained assuming that detrapping from deep trap states is slow compared to the scan rate of V [46]. In the cathodic direction V decreases, and the electron Fermi level rises; when its value is close to ε_{mts} the monoenergetic trap states are occupied, which causes the observed peak in C = dQ/dV. However, slow detrapping (thus slow variation of the charge accommodated in the deep trap states) results in a much smaller capacitive effect in the anodic direction. In the present article, the model assumes fast detrapping, and predicts a perfectly symmetric behaviour in the charging and discharging directions. The fitted values of E_{mts} show no remarkable dependence on the TiO_2 layer thickness. Their values for the different fabrication protocols are shown in Table 2.

Regarding the interpretation of the R_F term, R_{Fa} shows extremely high values, characteristic of an isolator ($R_{Fa} > 10^{11}$ Ω). For positive or small absolute values of V_{app}, the term

Please cite this article as: Ansón-Casaos A et al., Modelling TiO_2 photoanodes for PEC water splitting: Decoupling the influence of intrinsic material properties and film thickness, International Journal of Hydrogen Energy, https://doi.org/10.1016/j.ijhydene.2023.06.284

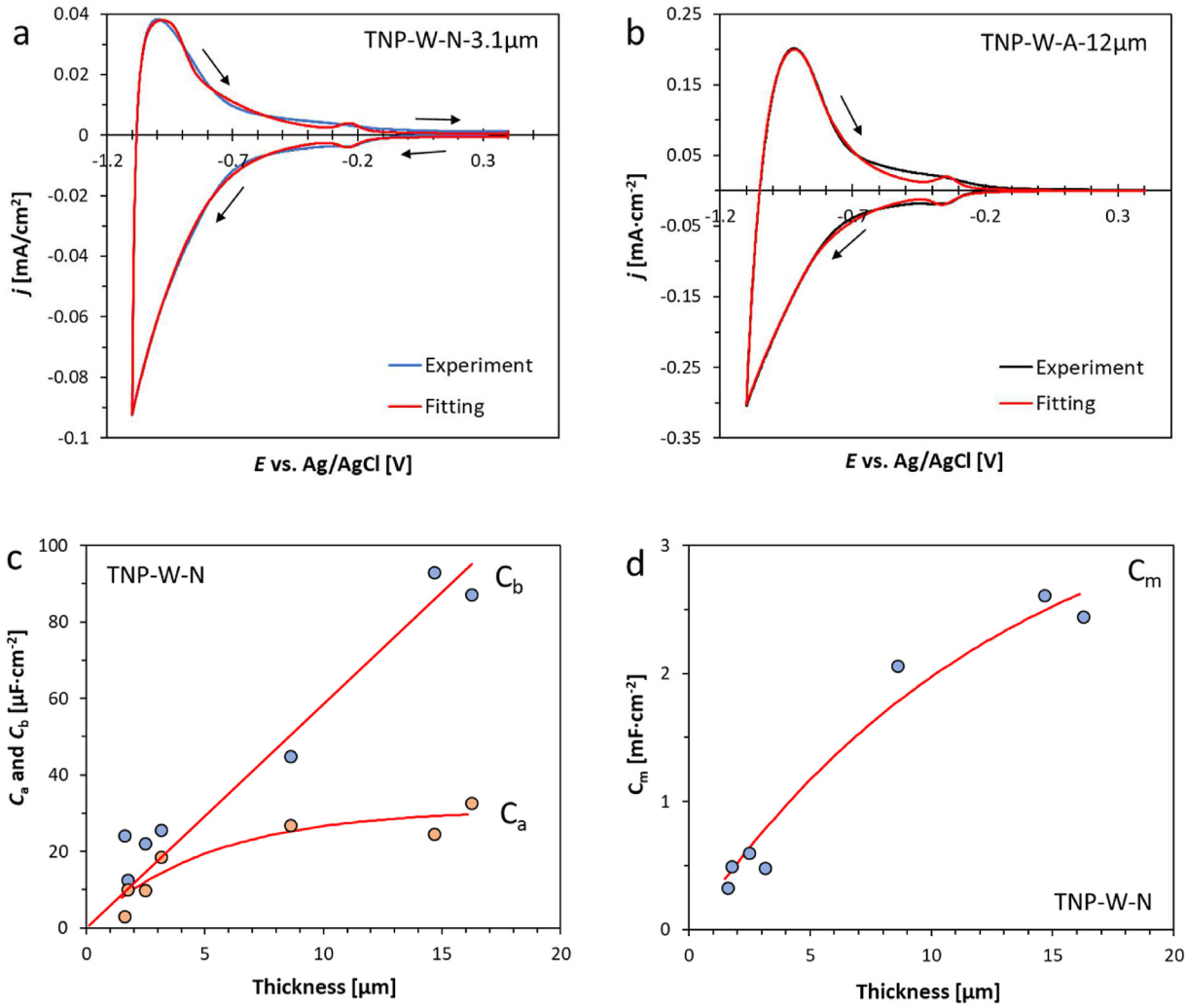

Fig. 4 – The fitting outcome of CV experiments in the dark: a, b) comparison of experimental data and mathematical fitting on TiO_2 film electrodes of two different thicknesses; c, d) trends for the C_a, C_b and C_m fitting parameters as functions of electrode thickness in the TNP-W-N series.

$R_{Fa}\cdot\exp(\alpha_R V_{app}/V_T)$ overwhelms R_{Fb}, and thus the faradaic current is virtually zero. For a sufficiently negative V_{app}, the predominant term becomes R_{Fb}, whose value allows for a non-negligible current. R_{Fb} can be fitted to a decreasing exponential function of the thickness (Table 2). Its values in the charge accumulation region (E < −1 V vs. Ag/AgCl) are in the range of 10^4–10^5 Ω. Accordingly, the current through R_F becomes non-negligible for voltages V < −0.5 V and reaches a maximum value in the order of 10 $\mu A\ cm^{-2}$ at V = −1.1 V. Such maximum values only represent between 11% and 27% of the total, while most of the current is linked to the capacitance term.

Lastly, the results of electrochemical impedance spectroscopy (EIS) measurements were fitted to a simplified equivalent circuit (Fig. 5, Table 2), which essentially includes the CV model circuit of Fig. 1 c. The range of calculated values for R_s and C from EIS and CV exhibits good agreement (Table 3). The results also evidence that R_s does not depend on the thickness of the film.

In analyzing the effects of the sintering atmosphere on model parameters (Table 2), we identify significant potential changes in α_c and R_s (Table 2). Specifically, the TNP-W-N series exhibit higher α_c values compared to the air-sintered electrodes. This high α_c value, which is linked to the distribution of continuous trap states beneath the conduction band, suggests an increased abundance of electron states near the band edge while concurrently reducing the number of deep states within the band-gap. We hypothesize that this alteration in the DOS may be coupled to the presence of oxygen vacancies resulting from the sintering treatment performed under a nitrogen atmosphere. Additionally, another noteworthy effect is the decrease in the R_s value, which refers to the electrolyte side according to the model. This decline indicates an indirect improvement in charge carrier mobility nearby the electrode surface. However, when considering the remaining model parameters, the effects of the sintering atmosphere fall within the range of experimental error.

Please cite this article as: Ansón-Casaos A et al., Modelling TiO_2 photoanodes for PEC water splitting: Decoupling the influence of intrinsic material properties and film thickness, International Journal of Hydrogen Energy, https://doi.org/10.1016/j.ijhydene.2023.06.284

Table 2 – Fitting parameters from CV measurements in the dark. Series TNP-W-N and TNP-W-A include coefficients to calculate the model parameters as a function of the sample thickness (Eqs. (14)–(16)).

Parameter		TNP-I-A	TNP-W-N	TNP-W-A
E_{mts} [V]		-0.396 ± 0.001	-0.38 ± 0.08	-0.26 ± 0.06
Constant throughout the series				
α_c		0.114 ± 0.002	0.148 ± 0.012	0.128 ± 0.012
α_R		0.039 ± 0.002	0.55 ± 0.10	0.71 ± 0.23
R_s [$\Omega \cdot cm^2$]		437 ± 164	278 ± 70	720 ± 60
$p = p_0 \cdot h/L_0$				
C_b [$F \cdot cm^{-2}$]		$8.6 \cdot 10^{-6} \pm 8 \cdot 10^{-7}$		
	$C_{b,0}$ [$F \cdot cm^{-2}$]		$5.8 \cdot 10^{-6} \pm 3.7 \cdot 10^{-6}$	$7.4 \cdot 10^{-6} \pm 9 \cdot 10^{-7}$
	r^2_b		0.97	0.92
$p = p_0 (1 - \exp(-h/L_p))$				
C_a [$F \cdot cm^{-2}$]		$1.79 \cdot 10^{-5} \pm 2 \cdot 10^{-7}$		
	$C_{a,0}$ [$F \cdot cm^{-2}$]		$3.1 \cdot 10^{-5} \pm 4 \cdot 10^{-6}$	$6.2 \cdot 10^{-5} \pm 1.7 \cdot 10^{-5}$
	L_a [μm]		5.0 ± 1.7	3.6 ± 2.3
	r^2_a		0.852	0.867
C_m [$F \cdot cm^{-2}$]		$7.5 \cdot 10^{-4} \pm 2 \cdot 10^{-5}$		
	$C_{m,0}$ [$F \cdot cm^{-2}$]		$3.7 \cdot 10^{-3} \pm 9.8 \cdot 10^{-3}$	$4.5 \cdot 10^{-3} \pm 8 \cdot 10^{-4}$
	L_m [μm]		13.3 ± 5.8	11.5 ± 3.5
	r^2_m		0.96	0.89
$p = p_0 \cdot \exp(-h/L_p)$				
R_{Fb} [$\Omega \cdot cm^2$]		$7.8 \cdot 10^3 \pm 5 \cdot 10^2$		
	$R_{Fb,0}$ [$\Omega \cdot cm^2$]		$1.3 \cdot 10^5 \pm 3 \cdot 10^4$	$1.7 \cdot 10^5 \pm 4 \cdot 10^4$
	L_{Fb} [μm]		5.5 ± 2.4	6.7 ± 3.9
	r^2_{Fb}		0.85	0.87

The CV measurements under light irradiation reflect very complex phenomena taking place in the electrode. Models for linear sweep voltammetry have been tested by different groups [47–51]. However, the interpretation of CV measurements under irradiation requires further attention in future research.

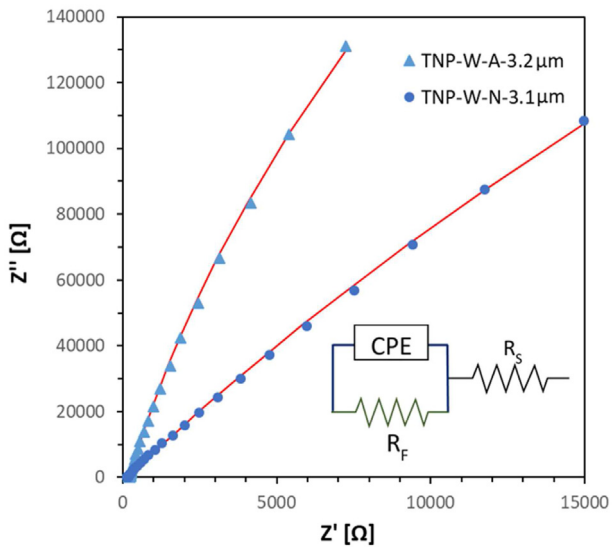

Fig. 5 – Nyquist plot from EIS data at 0.4 V vs. Ag/AgCl for two selected electrodes: TNP-W-N-3.1 μm and TNP-W-A-3.2 μm. Line fittings were performed considering the simplified circuit in the inset. A constant phase element (CPE) with impedance $Z_{CPE} = \frac{1}{Q(j\omega)^n}$ accounts for the non-ideality of the total capacitance (for an ideal capacitor, n = 1) [33]. The obtained values for the exponent are n > 0.9.

Transient photocurrent

Let us first consider the moment when the light is switched on (Fig. 6). We calculated the parameters by minimizing an error function analogous to Eq. (13), where J_{estim} is J_{spike} (Eq. (11)). The obtained values of τ_0 are similar for all the pulses of a sample, but they differ between different samples, showing an increasing trend with thickness (Fig. 7). Reasonably, the switching-on process involves charge carrier generation next to the irradiated surface and transport through the bulk TiO_2 layer, resulting in a thickness-dependent response.

To analyze the subsequent plateau, we proceeded in an analogous way, taking J_{estim} as $J_{plateau}$ (Eq. (12)). When the electrodes are fitted separately, the values for τ_1 and τ_2 show a remarkably weak dependence on thickness (Fig. 7). Unlike the switching-on process, relaxation phenomena at the stationary regime would be mainly associated to charge trapping and recombination in the bulk semiconductor, which would not be dependent on the length path through the material. This fact is in good agreement with the discussion by Gosh et al., assigning the origin of the relaxation to electron trapping [15].

The previous results led us to formulate the following working hypothesis: τ_1 and τ_2 depend only on the intrinsic material properties and τ_0 is a characteristic feature of each sample thickness, while the remaining parameters account

Table 3 – Comparison of calculated values of C (= $C_{cts} + C_{mts} + C_b$) and R_s from CV and EIS data fitting.

	R_s [$\Omega \cdot cm^2$]		C range [$\mu F \cdot cm^{-2}$]	
Series	CV	EIS	CV	EIS
TNP-W-N	278 ± 70	144 ± 39	18–124	38–110
TNP-W-A	720 ± 60	225 ± 74	13–100	43–63

Please cite this article as: Ansón-Casaos A et al., Modelling TiO_2 photoanodes for PEC water splitting: Decoupling the influence of intrinsic material properties and film thickness, International Journal of Hydrogen Energy, https://doi.org/10.1016/j.ijhydene.2023.06.284

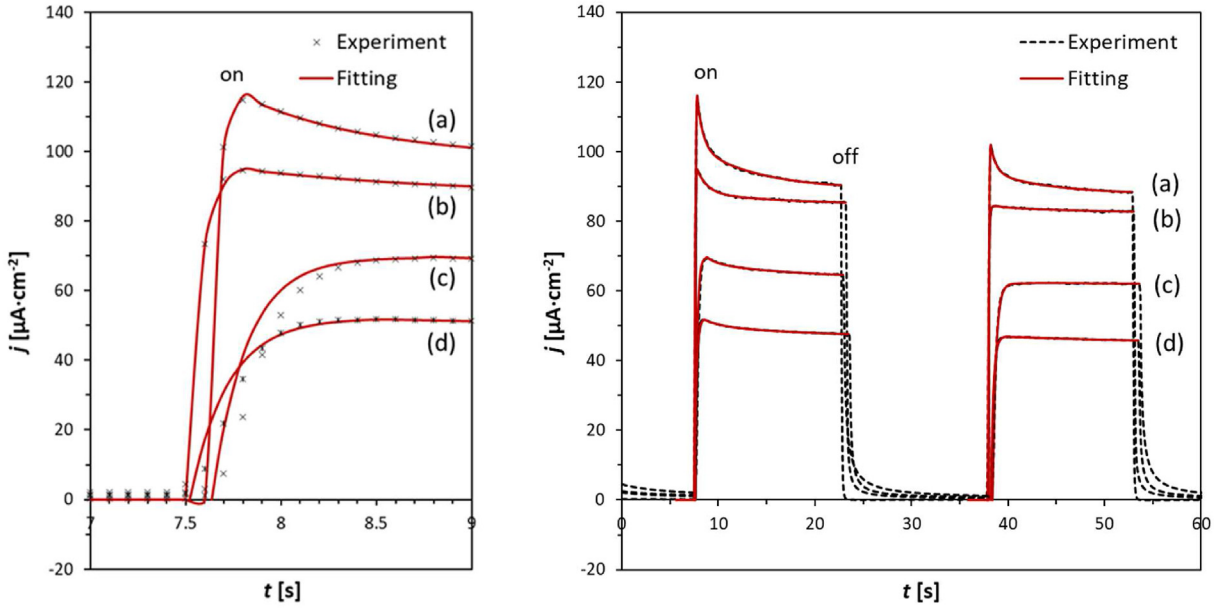

Fig. 6 – Comparison between experimental data and fitting outcome for the two first pulses of transient photocurrent measurements on four electrodes: a) TNP-I-A-2.0 μm; b) TNP-W-N-3.1 μm; c) TNP-W-N-8.6 μm; and d) TNP-W-A-3.2 μm. Left panel shows in detail the rise part of the first pulse.

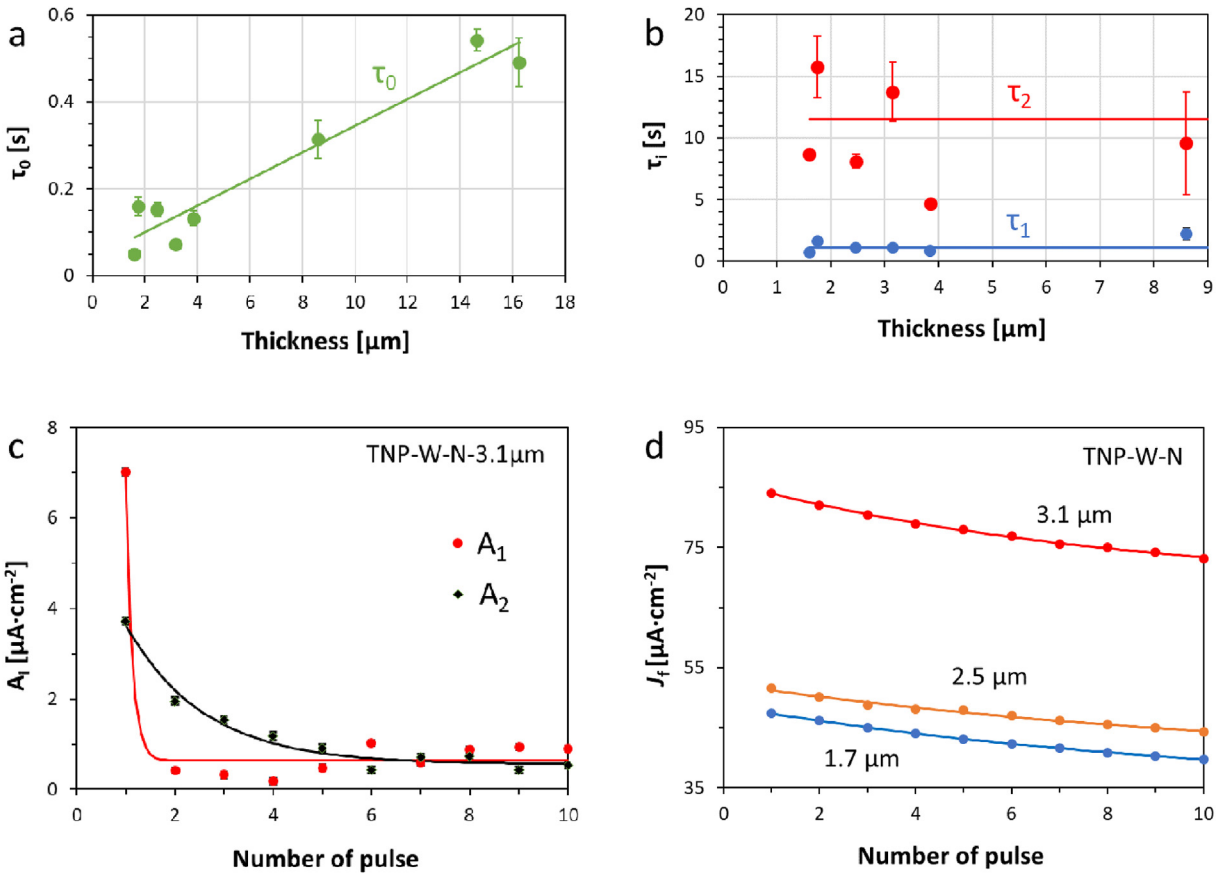

Fig. 7 – Identification of trends in the fitting parameters obtained from transient photocurrent measurements: a) τ_0 and b) τ_1 and τ_2 at different thicknesses for the electrode series TNP-W-N; c) A_i (i = 1, 2) vs. Number of pulse for the sample electrode TNP-W-N-3.1 μm; and d) J_f vs Number of pulse for three samples of the series TNP-W-N.

Please cite this article as: Ansón-Casaos A et al., Modelling TiO_2 photoanodes for PEC water splitting: Decoupling the influence of intrinsic material properties and film thickness, International Journal of Hydrogen Energy, https://doi.org/10.1016/j.ijhydene.2023.06.284

Table 4 – Fitting parameters from transient photocurrent measurements. Values of J_{f0} for the TNP-W-N and TNP-W-A series correspond to the sample providing the largest photocurrent (thickness around 3 μm).

Parameter	TNP-I-A	TNP-W-N	TNP-W-A
$<\tau_0>$ [s]	0.07 ± 0.04	0.24 ± 0.18	0.30 ± 0.15
τ_1 [s]	0.60 ± 0.01	1.10 ± 0.02	1.86 ± 0.05
τ_2 [s]	6.37 ± 0.12	10.1 ± 0.4	17.9 ± 1.9
J_{f0} [μA·cm^{-2}]	78.2 ± 1.4	74.8 ± 0.8	37.7 ± 0.8

for the variance of behaviour observed for different photopulses and electrode thicknesses. We checked the hypothesis by forcing common values of the pair $\{\tau_1, \tau_2\}$ for all of the pulses and all of the samples in a series. On the other hand, we forced a common value of τ_0 for all of the pulses of the same sample. Numerical results give support to our working hypothesis. The goodness of the fit is estimated by both visual inspection (see Fig. 6) and comparing the value of the error function (Eq. (13)) with that computed when no restrictions are imposed to the parameters.

Table 4 summarizes our results, including values of τ_i and their standard deviations $\sigma(\tau_i)$ for each group of electrodes. As τ_0 differs between different thickness electrodes in the series, we show its average value. Note the small values of $\sigma(\tau_1), \sigma(\tau_2)$ and the larger values for $\sigma(\tau_0)$, reflecting that the formers are indeed common to all the samples in a series. Logically, $\tau_0 < \tau_1 < \tau_2$. Also, τ_i (TNP-I-A) < τ_i (TNP-W-N) < τ_i (TNP-W-A), indicating that the kinetics of those physical phenomena depend on the processing conditions. The fabrication protocol can influence many characteristics of the TiO_2 layer, including particle aggregation, porosity, roughness, connectivity and surface chemistry.

In addition, values of J_F, A_1 and A_2 are sample and pulse dependent. Their values for the 10 pulses of an electrode sample can be fitted to exponential decays (Fig. 7c and d). In particular, A_1 and A_2 attenuate through successive pulses, but at a very different rate. In the first pulse $A_1 > A_2$, while the subsequent attenuation is much faster for A_1. This suggests that the relaxation phenomenon with the smallest characteristic time (τ_1) is predominant in the first pulse, and immediately loses relevance when compared to the one with largest characteristic time.

We are interested in the stationary photocurrent, given by J_F in Eq. (12). To estimate it for each sample, we analyze the trend of J_f values through the consecutive pulses, which can be fitted by an exponential decay: $J_f \sim J_{f0} + B \bullet e^{-N_p/P}$, N_p being the number of pulse and P an adjustable parameter. J_{f0} is the stationary value of J_f, reached after a long enough time. It is thickness-dependent, showing a steep rise for thickness up to approximately 3 μm, and a slow decay for thicker samples. Estimations of the maximum stationary values are provided in Table 4. Physically, the presence of a photocurrent maximum is typically explained as a balance considering light accessibility, availability of charge generation centers, carrier mobility and transport, charge transfer and recombination. Those phenomena depend on a spatial dimension, which is limited by the thickness.

Conclusions

Experimental PEC techniques are utilized to characterize a set of TiO_2 photoanodes, including three groups of samples in terms of their fabrication protocol and a series of different TiO_2 layer thickness. The experimental data-set of CV in the dark and transient photocurrent is described and interpreted according to physical and mathematical models.

Qualitatively, we assess the validity and limitations of the models, and expand them to be able to consider thickness effects. The physicochemical phenomena that are responsible for CV characteristics in the dark are relatively well understood. In a series of electrodes with different thickness, we can distinguish between those parameters that follow defined trends with thickness and others that are independent of thickness. In examining the electrode sintering atmosphere, it becomes evident that two parameters (α_c and R_s), which are independent of thickness, exhibit a diversified influence. Transient photocurrent measurements are successfully fitted to an increasing inverse exponential function and a double exponential decay. These findings are accompanied by a series of characteristic times (τ_i), which are linked to the kinetics of various photo-induced processes. Consequently, it is concluded that when modeling real photoelectrodes, the thickness variable must be taken into careful consideration.

Quantitatively, the analysis of parameter trends allows us to estimate their values as functions of the thickness, leading to a decrease in the number of free fitting parameters, and thus providing new insights on their physical meaning.

Declaration of competing interest

The authors declare that they have no known competing financial interests or personal relationships that could have appeared to influence the work reported in this paper.

Acknowledgements

Special thanks are directed to Javier Soler Gil for his help with electrode preparation and photoelectrochemical measurements. Authors would like to acknowledge the use of Servicio General de Apoyo a la Investigación-SAI, Universidad de Zaragoza. Financial support from Spanish MICINN/AEI under projects PID2019-104272RB-C51/AEI/10.13039/501100011033 and PID2019-104307 GB-100, and the Diputación General de Aragón under projects T03_23R and E47_23R (Grupos Reconocidos) is acknowledged.

REFERENCES

[1] Ros C, Andreu T, Morante JR. Photoelectrochemical water splitting: a road from stable metal oxides to protected thin film solar cells. J Mater Chem 2020;8:10625–69. https://doi.org/10.1039/d0ta02755c.

[2] Minggu LJ, Daud WRW, Kassim MB. An overview of photocells and photoreactors for photoelectrochemical water splitting. Int J Hydrogen Energy 2010;35:5233–44. https://doi.org/10.1016/j.ijhydene.2010.02.133.
[3] Carver C, Ulissi Z, Ong CK, Dennison S, Kelsall GH, Hellgardt K. Modelling and development of photoelectrochemical reactor for H_2 production. Int J Hydrogen Energy 2012;37:2911–23. https://doi.org/10.1016/j.ijhydene.2011.07.012.
[4] Tilley SD. Recent advances and emerging trends in photo-electrochemical solar energy conversion. Adv Energy Mater 2019;9:1802877. https://doi.org/10.1002/aenm.201802877.
[5] Pinaud BA, Benck JD, Seitz LC, Forman AJ, Chen Z, Deutsch TG, et al. Technical and economic feasibility of centralized facilities for solar hydrogen production via photocatalysis and photoelectrochemistry. Energy Environ Sci 2013;6:1983–2002. https://doi.org/10.1039/c3ee40831k.
[6] Sathre R, Greenblatt JB, Walczak K, Sharp ID, Stevens JC, Ager JW, et al. Opportunities to improve the net energy performance of photoelectrochemical water-splitting technology. Energy Environ Sci 2016;9:803–19. https://doi.org/10.1039/c5ee03040d.
[7] Grimm A, de Jong WA, Kramer GJ. Renewable hydrogen production: a techno-economic comparison of photoelectrochemical cells and photovoltaic-electrolysis. Int J Hydrogen Energy 2020;45:22545–55. https://doi.org/10.1016/j.ijhydene.2020.06.092.
[8] Nandjou F, Haussener S. Modeling the photostability of solar water-splitting devices and stabilization strategies. ACS Appl Mater Interfaces 2022;14:43095–108. https://doi.org/10.1021/acsami.2c08204.
[9] Monllor-Satoca D, Díez-García MI, Lana-Villarreal T, Gómez R. Photoelectrocatalytic production of solar fuels with semiconductor oxides: materials, activity and modeling. Chem Commun 2020;56:12272–89. https://doi.org/10.1039/d0cc04387g.
[10] Fabregat-Santiago F, Mora-Seró I, Garcia-Belmonte G, Bisquert J. Cyclic voltammetry studies of nanoporous semiconductors. Capacitive and reactive properties of nanocrystalline TiO_2 electrodes in aqueous electrolyte. J Phys Chem B 2003;107:758–68. https://doi.org/10.1021/jp0265182.
[11] Berger T, Monllor-Satoca D, Jankulovska M, Lana-Villarreal T, Gómez R. The electrochemistry of nanostructured titanium dioxide electrodes. ChemPhysChem 2012;13:2824–75. https://doi.org/10.1002/cphc.201200073.
[12] Liu B, Zhao X, Yu J, Parkin IP, Fujishima A, Nakata K. Intrinsic intermediate gap states of TiO_2 materials and their roles in charge carrier kinetics. J Photochem Photobiol C Photochem Rev 2019;39:1–57. https://doi.org/10.1016/j.photochemrev.2019.02.001.
[13] Peter LM. Energetics and kinetics of light-driven oxygen evolution at semiconductor electrodes: the example of hematite. J Solid State Electrochem 2013;17:315–26. https://doi.org/10.1007/s10008-012-1957-3.
[14] Peter LM, Walker AB, Bein T, Hufnagel AG, Kondofersky I. Interpretation of photocurrent transients at semiconductor electrodes: effects of band-edge unpinning. J Electroanal Chem 2020;872:114234. https://doi.org/10.1016/j.jelechem.2020.114234.
[15] Ghosh NG, Sarkar A, Zade SS. The type-II n-n inorganic/organic nano-heterojunction of Ti^{3+} self-doped TiO_2 nanorods and conjugated co-polymers for photoelectrochemical water splitting and photocatalytic dye degradation. Chem Eng J 2021;407:127227. https://doi.org/10.1016/j.cej.2020.127227.
[16] Hernández S, Saracco G, Barbero G, Alexe-Ionescu AL. Role of the electrode morphology on the optimal thickness of $BiVO_4$ anodes for photoelectrochemical water splitting cells. J Electroanal Chem 2017;799:481–6. https://doi.org/10.1016/j.jelechem.2017.06.057.
[17] Murakami N, Watanabe R. Simultaneous measurements of photoabsorption and photoelectrochemical performance for thickness optimization of a semiconductor photoelectrode. ACS Comb Sci 2020;22:791–5. https://doi.org/10.1021/acscombsci.0c00113.
[18] Jiang X, Cheng X, Zhang Z, Chen T, Tao K, Han W. Computation-assisted performance optimization for photoelectrochemical photoelectrodes. Appl Phys Lett 2022;120:063901. https://doi.org/10.1063/5.0080794.
[19] Seferlis AK, Neophytides SG. On the kinetics of photoelectrocatalytic water splitting on nanocrystalline TiO_2 films. Appl Catal B Environ 2013;132–133:543–52. https://doi.org/10.1016/j.apcatb.2012.12.016.
[20] Altomare M, Lee K, Killian MS, Selli E, Schmuki P. Ta-doped TiO_2 nanotubes for enhanced solar-light photoelectrochemical water splitting. Chem Eur J 2013;19:5841–4. https://doi.org/10.1002/chem.201203544.
[21] Park J-J, Kim D-Y, Lee J-G, Cha Y-H, Swihart MT, Yoon SS. Supersonic aerosol-deposited TiO_2 photoelectrodes for photoelectrochemical solar water splitting. RSC Adv 2014;4:8661–70. https://doi.org/10.1039/c3ra47998f.
[22] Ibadurrohman M, Hellgardt K. Morphological modification of TiO_2 thin films as highly efficient photoanodes for photoelectrochemical water splitting. ACS Appl Mater Interfaces 2015;7:9088–97. https://doi.org/10.1021/acsami.5b00853.
[23] Terashima C, Hishinuma R, Roy N, Sugiyama Y, Latthe SS, et al. Charge separation in TiO_2/BDD heterojunction thin film for enhanced photoelectrochemical performance. ACS Appl Mater Interfaces 2016;8:1583–8. https://doi.org/10.1021/acsami.5b10993.
[24] Matarrese R, Nova I, Li Bassi A, Casari CS, Russo V, Palmas S. Preparation and optimization of TiO_2 photoanodes fabricated by pulsed laser deposition for photoelectrochemical water splitting. J Solid State Electrochem 2017;21:3139–54. https://doi.org/10.1007/s10008-017-3639-7.
[25] Phoon BL, Pan GT, K Yang TC, Lee KM, Lai CW, Juan JC. Facile preparation of nanocrystalline TiO_2 thin films using electrophoretic deposition for enhancing photoelectrochemical water splitting response. J Mater Sci Mater Electron 2017;28:16244–53. https://doi.org/10.1007/s10854-017-7528-8.
[26] Gardecka AJ, Bishop C, Lee D, Corby S, Parkin IP, Kafizas A, et al. High efficiency water splitting photoanodes composed of nano-structured anatase-rutile TiO_2 heterojunctions by pulsed-pressure MOCVD. Appl Catal B Environ 2018;224:904–11. https://doi.org/10.1016/j.apcatb.2017.11.033.
[27] Günnemann C, Curti M, Eckert JG, Schneider J, Bahnemann DW. Tailoring the photoelectrochemical activity of TiO_2 electrodes by multilayer screen-printing. ChemCatChem 2019;11:6439–50. https://doi.org/10.1002/cctc.201901872.
[28] Scandola L, Latorrata S, Matarrese R, Cristiani C, Nova I. Effect of thickness and cracking phenomena on the photocatalytic performances of Ti/TiO_2 photoanodes produced by dip coating. Mater Chem Phys 2019;234:1–8. https://doi.org/10.1016/j.matchemphys.2019.05.074.
[29] Gent E, Taffa DH, Wark M. Multi-layered mesoporous TiO_2 thin films: photoelectrodes with improved activity and stability. Coatings 2019;9:625. https://doi.org/10.3390/coatings9100625.
[30] Yang H, Kim E, Kim SH, Jeong MS, Shin H. Hole trap, charge transfer and photoelectrochemical water oxidation in thickness-controlled TiO_2 anatase thin films. Appl Surf Sci

Please cite this article as: Ansón-Casaos A et al., Modelling TiO_2 photoanodes for PEC water splitting: Decoupling the influence of intrinsic material properties and film thickness, International Journal of Hydrogen Energy, https://doi.org/10.1016/j.ijhydene.2023.06.284

2020;529:147020. https://doi.org/10.1016/j.apsusc.2020.147020.
[31] Sharma P, Kumar P, Deva D, Shrivastav R, Dass S, Satsangi VR. Nanostructured Zn-Fe_2O_3 thin film modified by Fe-TiO_2 for photoelectrochemical generation of hydrogen. Int J Hydrogen Energy 2010;35:10883–9. https://doi.org/10.1016/j.ijhydene.2010.07.016.
[32] Stepanovich A, Sliozberg K, Schuhmann W, Ludwig A. Combinatorial development of nanoporous WO_3 thin film photoelectrodes for solar water splitting by dealloying of binary alloys. Int J Hydrogen Energy 2012;37:11618–24. https://doi.org/10.1016/j.ijhydene.2012.05.039.
[33] Lopes T, Andrade L, Le Formal F, Gratzel M, Sivula K, Mendes A. Hematite photoelectrodes for water splitting: evaluation of the role of film thickness by impedance spectroscopy. Phys Chem Chem Phys 2014;16:16515–23. https://doi.org/10.1039/c3cp55473b.
[34] Hernández S, Thalluri SM, Sacco A, Bensaid S, Saracco G, Russo N. Photo-catalytic activity of $BiVO_4$ thin-film electrodes for solar-driven water splitting. Appl Catal, A 2015;504:266–71. https://doi.org/10.1016/j.apcata.2015.01.019.
[35] Sharma D, Satsangi VR, Shrivastav R, Waghmare UV, Dass S. Understanding the Photoelectrochemical properties of nanostructured CeO_2/Cu_2O heterojunction photoanode for efficient photoelectrochemical water splitting. Int J Hydrogen Energy 2016;41:18339–50. https://doi.org/10.1016/j.ijhydene.2016.08.079.
[36] Tolod KR, Hernandez S, Castellino M, Deorsola FA, Davarpanah E, Russo N. Optimization of $BiVO_4$ photoelectrodes made by electrodeposition for sun-driven water oxidation. Int J Hydrogen Energy 2020;45:605–18. https://doi.org/10.1016/j.ijhydene.2019.10.236.
[37] Abdelmoneim A, Naji A, Wagenaars E, Shaban M. Outstanding stability and photoelectrochemical catalytic performance of (Fe, Ni) co-doped Co_3O_4 photoelectrodes for solar hydrogen production. Int J Hydrogen Energy 2021;46:12915–35. https://doi.org/10.1016/j.ijhydene.2021.01.113.
[38] Xiao J, Peng L, Gao L, Zhong J, Huang Z, Yuan E, et al. Improving light absorption and photoelectrochemical performance of thin-film photoelectrode with a reflective substrate. RSC Adv 2021;11:16600–7. https://doi.org/10.1039/d1ra02826j.
[39] Ansón-Casaos A, Sampaio MJ, Jarauta-Córdoba C, Martínez MT, Silva CG, Faria JL, et al. Evaluation of sol-gel TiO_2 photocatalysts modified with carbon or boron compounds and crystallized in nitrogen or air atmospheres. Chem Eng J 2015;277:11–20. https://doi.org/10.1016/j.cej.2015.04.136.
[40] Cano-Casanova L, Ansón-Casaos A, Hernández-Ferrer J, Benito AM, Maser WK, Garro N, et al. Surface-enriched boron-doped TiO_2 nanoparticles as photocatalysts for propene oxidation. ACS Appl Nano Mater 2022;5:12527–39. https://doi.org/10.1021/acsanm.2c02217.
[41] Ansón-Casaos A, Hernández-Ferrer J, Rubio-Muñoz C, Santidrian A, Martínez MT, Benito AM, et al. Electron trap states and photopotential of nanocrystalline titanium dioxide electrodes filled with single-walled carbon nanotubes. Chemelectrochem 2017;4:2300–7. https://doi.org/10.1002/celc.201700321.
[42] Bisquert J, Cendula P, Bertoluzzi L, Gimenez S. Energy diagram of semiconductor/electrolyte junctions. J Phys Chem Lett 2014;5:205–7. https://doi.org/10.1021/jz402703d.
[43] Jankulovska M, Berger T, Wong SS, Gómez R, Lana-Villarreal T. Trap states in TiO_2 films made of nanowires, nanotubes or nanoparticles: an electrochemical study. ChemPhysChem 2012;13:3008–17. https://doi.org/10.1002/cphc.201200072.
[44] de Araújo MA, Gromboni MF, Marken F, Parker SC, Peter LM, Turner J, et al. Contrasting transient photocurrent characteristics for thin films of vacuum-doped "grey" TiO_2 and "grey" Nb_2O_5. Appl Catal B Environ 2018;237:339–52. https://doi.org/10.1016/j.apcatb.2018.05.065.
[45] Marquadt DW. An algorithm for least squares estimation of nonlinear parameters. SIAM J Appl Math 1963;11:431–41. https://doi.org/10.1137/0111030.
[46] Bertoluzzi L, Herraiz-Cardona I, Gottesman R, Zaban A, Bisquert J. Relaxation of electron carriers in the density of states of nanocrystalline TiO_2. J Phys Chem Lett 2014;5:689–94. https://doi.org/10.1021/jz4027584.
[47] Andrade L, Lopes T, Aguilar Ribeiro H, Mendes A. Transient phenomenological modeling of photoelectrochemical cells for water splitting e Application to undoped hematite electrodes. Int J Hydrogen Energy 2011;36:175–88. https://doi.org/10.1016/j.ijhydene.2010.09.098.
[48] Andrade L, Lopes T, Mendes A. Dynamic phenomenological modeling of PEC cells for water splitting under outdoor conditions. Energy Proc 2012;22:23–34. https://doi.org/10.1016/j.egypro.2012.05.227.
[49] Cendula P, Tilley SD, Gimenez S, Bisquert J, Schmid M, Grätzel M, et al. Calculation of the energy band diagram of a photoelectrochemical water splitting cell. J Phys Chem C 2014;118:29599–607. https://doi.org/10.1021/jp509719d.
[50] Miao B, Iqbal A, Bevan KH. Utilizing band diagrams to interpret the photovoltage and photocurrent in photoanodes: a semiclassical device modeling study. J Phys Chem C 2019;123:28593–603. https://doi.org/10.1021/acs.jpcc.9b07536.
[51] Hien TT, Quang ND, Kim C, Kim D. Energy diagram analysis of photoelectrochemical water splitting process. Nano Energy 2019;57:660–9. https://doi.org/10.1016/j.nanoen.2018.12.093.

Please cite this article as: Ansón-Casaos A et al., Modelling TiO_2 photoanodes for PEC water splitting: Decoupling the influence of intrinsic material properties and film thickness, International Journal of Hydrogen Energy, https://doi.org/10.1016/j.ijhydene.2023.06.284